

Monte Carlo Simulations of Ultrasound Scattering and Absorption in Finite-Size Heterogeneous Materials

Hao Zhou^{1,2}, Xiaoping Jia^{2,3,*}, Li-Yun Fu^{4,†} and Arnaud Tourin²

¹College of Information Engineering, Zhejiang University of Water Resources and Electric Power, Hangzhou 310018, China

²Institut Langevin, ESPCI Paris, Université PSL, CNRS, Paris 75005, France

³Université Gustave Eiffel, 77454 Marne-la-Vallée Cedex 2, France

⁴Key Laboratory of Deep Oil and Gas, China University of Petroleum, Qingdao 266580, China

 (Received 11 June 2021; revised 6 August 2021; accepted 9 August 2021; published 3 September 2021)

Determination of ultrasound scattering and intrinsic attenuations in heterogeneous media is of importance from material characterization to geophysical applications. Here, we present an efficient inverse method within a finite-size scattering medium, where boundary reflection plays a crucial role. To fit the energy profile of scattered coda waves, we solve the acoustic radiative-transfer equation by Monte Carlo simulations for cylinder and slab geometries, under the isotropic scattering approximation. We show that the fit with the simplistic radiative-transfer solution in an infinite medium may result in underestimated values of the scattering mean free path, l_s , and absorption, Q_i^{-1} , by up to 40%. Our main finding is anomalous transport behavior in thin slab samples, where the ballistic peak and the diffusionlike one are merged into one single peak. This anomalous behavior, related to a wave-focusing effect in the forward direction, can mislead the inverse process and lead to an overestimation of l_s by more than 200%. We compare simulated energy profiles with ultrasound envelopes obtained in a polycrystal-like granite slab from the ballistic to the diffusive regime. The l_s deduced from off-axis detections agrees with that estimated from the correlation length of the shear-wave velocity by structural imaging analysis.

DOI: [10.1103/PhysRevApplied.16.034009](https://doi.org/10.1103/PhysRevApplied.16.034009)

I. INTRODUCTION

Experimental studies suggest that seismic (elastic) wave attenuation is much more sensitive to changes in rock properties than that of the wave velocity [1]. Attenuation refers here to the intrinsic (i.e., anelastic) attenuation that converts seismic energy into heat, otherwise called absorption or dissipation. Absorption is challenging to measure, since seismic amplitudes may be affected by many factors [2]. This difficulty also exists in ultrasonic laboratory experiments on rock samples due to beam spreading, wave scattering, and boundary reflections. For quasi-homogeneous rocks, wave scattering may be ignored. Absorption can then be measured from the ballistic or reflected pulses, i.e., the coherent wave field [3,4]. However, these methods may overestimate absorption in heterogeneous rocks, since ballistic wave attenuation also includes scattering by wavelength-scale heterogeneities [5]. Moreover, in strong (multiple) scattering rocks, such as granite and gabbro [6], it is even challenging to identify correctly coherent pulses from scattered coda signals. Similar situations are

also encountered for nondestructive evaluation of heterogeneous materials in engineering applications in which diagnostic methods based on ultrasonic (or seismic) coda waves are developed [7–13], including diffusing-wave spectroscopy in the case of evolving media [14]. Here, we investigate the transition from the ballistic to the diffusive regime within acoustic (scalar) radiative-transfer (RT) theory, to disentangle scattering and intrinsic attenuations from ultrasound coda waves in finite-size heterogeneous media.

RT theory is a general scattering theory [15–19] based on a particle description of wave propagation (see discussion in Sec. II A). It is usually expressed in terms of the specific intensity, defined as the radiant power per unit area; solid angle; and frequency. The specific intensity obeys a Boltzmann-type differential equation called the radiative-transfer equation (RTE), which can be solved through Monte Carlo (MC) simulations [20–23]. Interestingly, such simulations can handle complex boundary conditions [22,23], which would be difficult, if not impossible, to treat through analytical methods. The generality of RT theory is critical for the attenuation inverse problem, since ultrasound scattering in rocks may lead to an intermediate regime between two limiting cases: the weak-scattering

*xiaoping.jia@espci.fr

†lfu@upc.edu.cn

regime, which is well described by a single-scattering analytical model [24,25], and the strong-scattering regime, where the RTE is asymptotically equivalent to the diffusion equation [26–28]. Nevertheless, applying MC simulations to describe wave propagation in finite-size rocks requires the boundary condition and the geometry of the source to be treated carefully.

Unlike the layered half-space model used in seismology, rock samples used in laboratory experiments are often shaped in cuboid, slab, or cylinder geometries to facilitate the experimental control of pressure, temperature, saturation, etc. [29,30]. As shown in optics [31–33], and later in seismology [23], boundary reflections from such a finite-size sample have to be considered properly to determine the transport parameters. For slablike polycrystals, this can be done based on the existing steady-state RTE solution, but the time-dependent RTE needs to be solved numerically [7,34]. For ultrasonic measurements in granite and gabbro, only the reflection of coherent elastic waves from the boundary was previously taken into account [35]. Here, we investigate the effect of boundary reflections in the multiple-scattering regime to infer adequately intrinsic and scattering attenuations (or elastic mean free path).

Furthermore, the ultrasonic source transducer is often a finite-size source (instead of a point source). When the source is large relative to the propagation distance, plane-wave source geometry can be assumed [8,36]. In this case, the energy profile can noticeably be broadened, and the peak value time is delayed. When the source is smaller than the travel distance [37], it may instead be treated as a point source. Here, we consider the source-size effect precisely in our MC simulations and study its influence on inversed attenuations.

In Sec. II, we review the scalar RTE and its time-dependent analytical solution and then describe the numerical resolutions of the RTE using MC simulations in the case of infinite media and finite-size media with boundary reflection. In Sec. III, we study the effect of a finite-size source. Particular attention is paid to the impact of boundary reflections and source sizes on the intrinsic attenuation, Q_i^{-1} , and the scattering mean free path, l_s , inferred from MC simulations. In Sec. IV, we compare the simulated energy profiles to experimental data obtained both in a confined dry granular medium and on granite (i.e., a polycrystal rock) for the purpose of the inverse problem.

II. MC SIMULATIONS OF RADIATION TRANSPORT FOR A POINT SOURCE

A. Radiative-transfer theory

Wave scattering in random heterogeneous media is common in natural materials and has been extensively modeled in many areas of physics, such as solid-state physics, optics and acoustics [38,39], as well as seismology [18]. The

basic idea is to model wave propagation in an ensemble (instead of specific) of random heterogeneous media [40]. RT theory can statistically model multiply scattered waves. This theory is based upon the assumption that randomly scattered waves have uncorrelated random phases. The superposition of these scattered waves may be incoherent, leading to a description of wave propagation, not in terms of field quantities, such as stress or displacement, but in terms of average intensity. As such, it, of course, cannot provide a full description of wave propagation, but it can accurately describe the ensemble-averaged energy densities [16].

The RTE can be derived in either of two ways. The simple phenomenological method relies upon energy-conservation considerations in a representative volume, consisting of discrete scatterers [41]. In this approach, the wave equation is used only to determine wave velocities and properties for single-scattering events that constitute the multiple-scattering process. One may also derive the RTE directly from the wave equation based on the Bourret approximation to the Bethe-Salpeter equation for the second moment of the wave field [19,39]. Therefore, unlike the Dyson equation for describing the mean field of scattered waves, the RTE only accounts for the intensity evolution of scattered waves and ignores their phase information, which matters in wave-interference phenomena.

The scalar RTE governs the dependence of position \mathbf{r} and time t on the average intensity, $I(\mathbf{r}, t; \hat{\mathbf{s}})$, radiated in the direction given by the unit vector $\hat{\mathbf{s}}$ (the so-called average specific intensity), which can be written as follows for isotropic scattering and a pulsed point source:

$$\begin{aligned} & \frac{1}{V} \frac{\partial}{\partial t} I(\mathbf{r}, t, \hat{\mathbf{s}}) + \hat{\mathbf{s}} \cdot \nabla I(\mathbf{r}, t, \hat{\mathbf{s}}) \\ &= - \left(\frac{1}{l_s} + \frac{1}{l_a} \right) \nabla I(\mathbf{r}, t, \hat{\mathbf{s}}) + \frac{1}{l_s} \int \frac{d\hat{\mathbf{s}}'}{\Omega_d} I(\mathbf{r}, t, \hat{\mathbf{s}}') \\ &+ \frac{1}{V} \delta(\mathbf{r}) \delta(t), \end{aligned} \quad (1)$$

where V is the acoustic wave velocity, l_s is the scattering mean free path, l_a is the absorption length, and Ω_d is the surface area of the unit sphere [17]. Under the isotropic scattering assumption, the average energy density, $E(\mathbf{r}, t) = I(\mathbf{r}, t)/V$, can be derived from the specific intensity, $I(\mathbf{r}, t, \hat{\mathbf{s}})$, integrated over all directions $\hat{\mathbf{s}}$ [17,18,42].

To obtain $I(\mathbf{r}, t)$ or $E(\mathbf{r}, t)$ from integrodifferential Eq. (1), it is useful to consider the contribution from different scattering events ($n = 0, 1, 2, \dots$), as for the Boltzmann equation in the kinetic theory of gases [17,42]:

$$E(\mathbf{r}, t) = E_0(\mathbf{r}, t) + \sum_n E_n(\mathbf{r}, t) (n \geq 1), \quad (2)$$

in which the first term, $E_0(\mathbf{r}, t) = W_0 G_0(\mathbf{r}, t)$, indicates the incident ballistic wave energy at receiver point \mathbf{r} , and the second term is the sum of scattered wave energies from all possible scatterer points, \mathbf{r}' , to receiver \mathbf{r} . Here, W_0 is the source energy and $G_0(\mathbf{r}, t) = \exp(-Vt/l_s)/(4\pi Vr^2)\delta(t-r/V)$ is the pulsed Green function; $n = 1$ corresponds to the first-order or single scattering and $n > 1$ to multiple scattering. In three-dimensional infinite media, an approximate solution is deduced analytically for the energy density [17]:

$$E(\mathbf{r}, t) = \frac{W_0 e^{-Vt[(1/l_s)+(1/l_a)]}}{V4\pi r^2} \delta\left(t - \frac{r}{V_0}\right) + \frac{(1-r^2/V^2 t^2)^{1/8}}{(4\pi l_s V t/3)^{3/2}} W_0 e^{-Vt[(1/l_s)+(1/l_a)]} \times G\left\{\frac{Vt}{l_s}\left[1 - \frac{r^2}{(Vt)^2}\right]^{3/4}\right\} H\left(t - \frac{r}{V}\right), \quad (3)$$

where $G(x) \approx \exp(x)(1 + 2.026/x)^{1/2}$ and H is the Heaviside function.

Figure 1 plots the energy-density profiles derived from Eq. (3) at different source-receiver distances, L , for a given scattering mean free path, l_s . It is important to notice that the shape of the energy-density profile at short times strongly depends on the ratio of L/l_s . As revealed by Paaschens [17], the time-dependent energy density at a small distance L ($\sim l_s$) from a point source is dominated by the ballistic peak due to unscattered radiation, while it exhibits two peaks at a larger distance L ($> 2.5l_s$): a ballistic peak at time $t_b = L/V$ and a diffusion peak at $t \sim L^2/D_0$ (with D_0 as

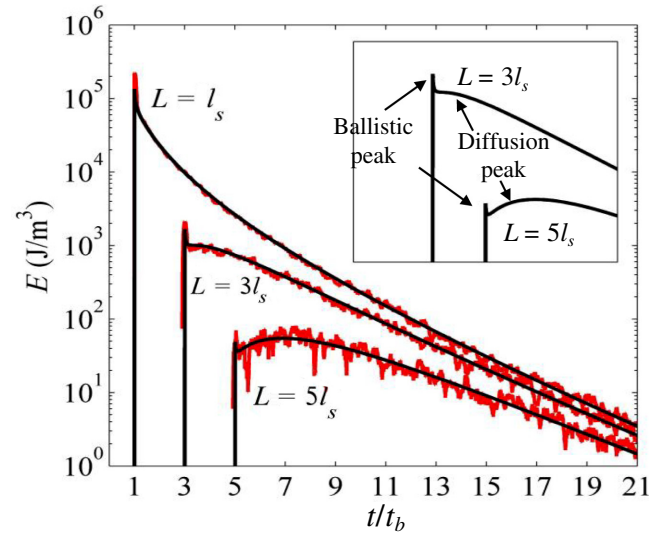


FIG. 1. Energy-density profiles in an infinite medium predicted by Eq. (3) at different source-receiver distances L (black curves) together with Monte Carlo simulations (red curves). $t_b = L/V$ is the ballistic arrival time. Inset reveals the presence of two peaks separated by a minimum in the energy density (see text).

the diffusion constant). The tail of the ballistic peak leads to a minimum in the energy density as a function of time due to single forward scattering ($n = 1$). As expected, we can recover the diffusion approximation at large L ($\geq 5l_s$).

In a finite-size three-dimensional medium with various boundaries, it is almost impossible to obtain the analytical solution of radiative transport. Instead, we may solve the RTE numerically through MC simulations.

B. Three-dimensional infinite media

The MC method has been used to model radiation transport in physics since the 1950s by simulating the random scattering of a large number of individual particles [43,44]. It was introduced to seismology by Gusev and Abubakirov [20], where seismic wavelets with random phases were considered as acoustic particles.

The principle of the simulation is illustrated in Fig. 2(a) for isotropic scattering. In the beginning, a particle is shot out of source O in a random direction and travels at a constant speed during time interval Δt . The take-off angle, ϑ_0 , and the azimuthal angle, ϕ_0 , are given by $\vartheta_0 = \cos^{-1}(1-2U_1)$ and $\phi_0 = 2\pi U_2$, respectively, where U_1 and U_2 are independent and uniformly chosen random values between zero and one. The occurrence of scattering is determined by comparing a uniformly chosen random number between zero and one, U_3 , to $\Delta t/t_s$, where $t_s = l_s/V$ is the mean free time. When $\Delta t/t_s \geq U_3$, the particle changes direction. New scattering angles (ϑ_1, ϕ_1) are then determined by $\vartheta_1 = \cos^{-1}(1-2U_4)$ and $\phi_1 = 2\pi U_5$, where U_4 and U_5 are independent and uniformly chosen random values between zero and one. By sequentially tracing the particle trajectory, with $\Delta t = t_s/10$ (to obtain a good compromise between accuracy and computational cost), a randomly walking particle is obtained.

The Monte Carlo method simulates a lot of such independent (noncolliding) randomly walking particles. The

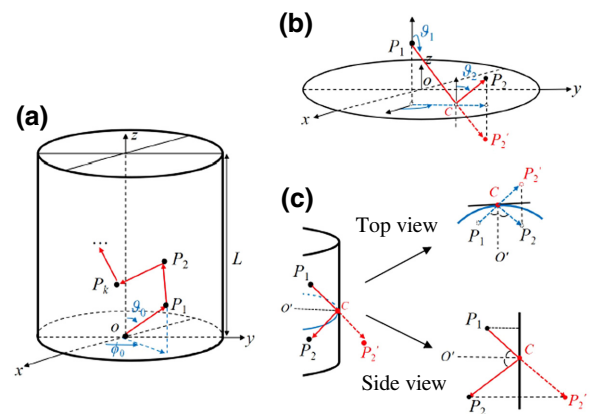


FIG. 2. (a) Random walking of particles (or radiation pulses) in a random medium. (b) Reflections at a flat surface (top and bottom) and (c) at a curved surface (lateral wall).

space-time energy density can then be obtained by counting the number of particles in a representative volume [45]. Say we shoot N particles simultaneously from the point source and each particle carries a unit energy ($W_0=1$ J), the particle number in a representative sphere at \mathbf{r} with a diameter $d_r (\ll l_s)$ is n . The absorption is modeled by multiplying $\exp(-\Delta t/t_a)$ to W_0 at every Δt , i.e., $W=W_0 \exp(-p \Delta t/t_a)$ with $t_a=l_a/V$ and $p=0, 1, 2, \dots$. Therefore, the energy density is determined to be $E(\mathbf{r}, p \Delta t) = n(\mathbf{r}, p \Delta t) W / (\pi d_r^3 / 6)$.

Figure 1 shows three simulated energy curves and the corresponding RTE solutions derived from Eq. (3) at $L=|\mathbf{r}_1|=l_s$, $|\mathbf{r}_2|=3l_s$, and $|\mathbf{r}_3|=5l_s$, for $N=10^7$, $V=450$ m/s, $f=1$ MHz, $Q_i=(2\pi l_a f)/V=500$, and $l_s=10^{-2}$ m. The simulated profiles coincide very well with the analytical RTE solutions in an infinite medium, which validates our numerical simulation.

The quality of the inversion of transport parameters l_s and Q_i essentially depends on the relevance of the model of wave transport in the medium (i.e., direct problem). Most of the works reported in the literature have focused on the energy-density profile at late times [33,46], behaving roughly as $E(t) \sim t^{-\gamma} \exp(-\omega t/Q)$, with γ as a constant [19,24]. Here, Q is the quality factor of coda waves, which may depend on both Q_i and Q_s (or l_s), as well as on boundary (internal) reflections [23,33] (see discussions in Sec. II C). From a practical point of view, Q_i and $Q_s (=2\pi l_s f/V)$ are then determined by a best fit to experimental coda envelopes (detected at different source-receiver distances, if applicable) with theoretical or MC simulated profiles, via a least-squares adjustment. If applicable, attenuation measurements of the direct, i.e., ballistic wave ($\sim Q_i^{-1} + Q_s^{-1}$) may complement those of coda decay to constrain Q_i and Q_s [46].

Note also that, in the diffusive regime, the transport mean free path, l^* ($\sim l_s$ for isotropic scattering), and the diffusion constant, $D (=Vl^*/3)$, can be adequately inferred from the early part of the energy-density profiles [8,36]. Such an inverse procedure based is followed here by monitoring the arrival of two peaks (ballistic and diffusion peaks) in the multiple-scattering regime [17,33].

C. Three-dimensional finite media

1. Boundary conditions

We now consider the random walking of particles inside a cylinder [Fig. 2(a)], which simulates isotropic wave scattering inside a solid cylinder surrounded by air, namely, that with a reflection coefficient of $R \approx 1$. Therefore, the pulsed radiation experiences perfect reflection at the boundaries considered here. To ensure that scattered energy remains inside the medium, we set $\vartheta_0 = U_1 \pi / 2$, which is slightly different from that in the above infinite medium, and $\phi_0 = 2\pi U_2$. Note, however, that the situation with partial reflection at the boundaries can be also

simulated by the Monte Carlo method. More specifically, Margerin *et al.* [23] and Hoshiba [22] have performed detailed investigations in a layered medium modeling the earth's crust and mantle.

There are two kinds of interfaces for the cylinder sample, i.e., planar surfaces on the top and bottom and a cylindrical lateral surface. The reflection of a particle at an interface obeys Snell's law. As shown in Fig. 2(b), this means that its new position, P_2 , after reflection is such that the distance P_1-C-P_2 is $V\Delta t$, ϑ_2 is equal to $(\pi - \vartheta_1)$, and the azimuthal angle is not changed ($\phi_1 = \phi_2$). When a particle is incident at the cylindrical surface, the latter is locally treated as a planar surface, according to the collision-point tangent plane. After reflection, the position of P_2 and the new direction (ϑ_2, ϕ_2) can then be calculated according to Snell's law, as seen from the top view and the side view in Fig. 2(c).

Implementing these principles, we can simulate wave-energy scattering in a finite-size heterogeneous medium for a pointlike source or a finite-size source (see Sec. II). By varying the source-receiver distance, L , versus the scattering mean free path, l_s , we may investigate the transition from the ballistic to the diffusive wave regime [33]. In the following, we fix $L (=10$ mm) and change the value of l_s (for different scattering materials) to consider different regimes of scattering. This protocol of simulation is a bit different from that used in Fig. 1, where l_s is fixed, as if working in the same scattering material but with a varying distance L .

2. Cylinder geometry

Figure 3 shows snapshots of the particles (illustrating radiation spreading) shot from a point source and recorded at two instants, t_1 and $t_2 (>t_1)$, in three cylindrical samples of the same length, $L=10$ mm, and diameter, $w (=L/4)=2.5$ mm, but of different scattering mean free paths, $l_s=L, L/3$, and $L/10$. Here, we use a common set of parameters: $V_0=450$ m/s and $Q_i=500$ (for $f=1$ MHz). From $t=0$ to $t=t_1 (=t_b/8$ with $t_b=L/V)$, the integrated outgoing particles form a hemisphere (coherent radiation front), with some randomly walking particles (incoherent radiation) behind. At instant $t_2 (=3/4 t_b)$, the integrated particle distribution includes boundary reflection of both the coherent front and randomly scattered particles [Figs. 3(a) and 3(b)]. The coherent radiation (hemispheric front) is reflected several times at an oblique incidence by the lateral wall (reverberations), before reaching the receiver at the opposite end. For $t \gg t_s (=l_s/V)$, the hemisphere dies out, so that the incoherent energy dominates [Fig. 3(c)], as expected, similar to the picture of wave scattering in infinite media.

Figure 4 depicts the simulated time-dependent averaged energy-density profiles, $E(t)$ (red curves), for the same three scattering samples (with different values of l_s but detected at the same source-receiver distance L). The

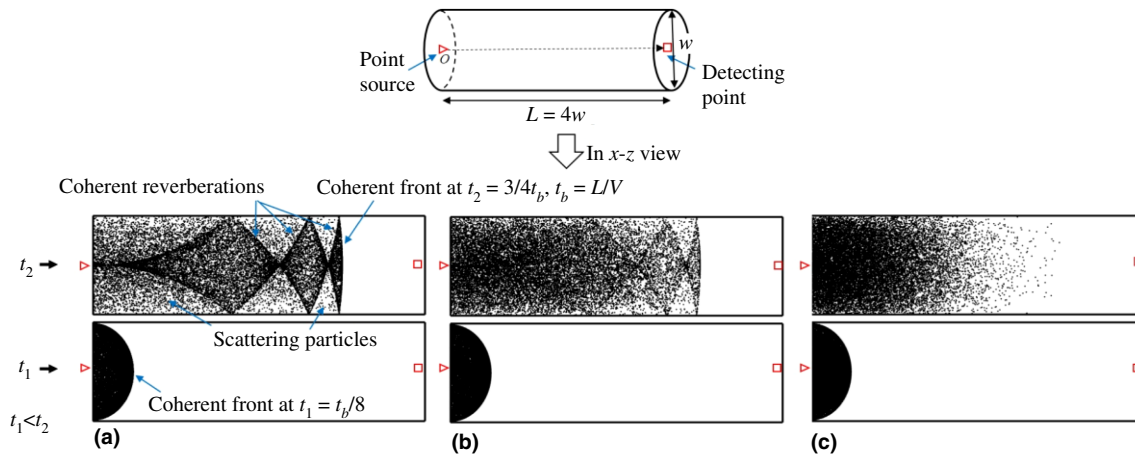


FIG. 3. MC simulations of radiation transport for a point source in a random medium with cylindrical geometry for three different scattering cylinders with (a) $L/l_s = 1$, (b) $L/l_s = 3$, and (c) $L/l_s = 10$. Snapshots are recorded at two instants, t_1 and t_2 .

corresponding energy-density profiles, $E(t)$, obtained in infinite media are given for comparison (black curves). They display the same shapes as those in Fig. 1(b) for equivalent ratios of $L/l_s = 1, 3$, and 10. As expected, both the detected energy levels are higher and the decaying rates at long times are slower in finite cylinders than in infinite media, since (perfect) boundary reflection, particularly at the lateral wall, prevents radiated energy from spreading and leakage. We also note that at short times the diffusion peak is a bit delayed compared with the infinite-medium case [Fig. 4(c)].

3. Slab geometry

Figure 5 displays similar snapshots of MC simulations for slabs with a width (diameter) of $w = 40 \text{ mm} = 4L$ (L is thickness). Unlike the cylindrical sample, from $t_1 = t_b$ to $t_2 = 2t_b$, the incoherent energy radiation is not reflected by the lateral wall. A small part of it is reflected from the top surface. As a result, incoherent energy transport in the slab

of $L/l_s = 10$ is very close to that in infinite media, as evidenced by the similarity of their energy-density profiles in Fig. 4(c) (blue and black curves). At long times, the signature of coherent reverberations tends to disappear, as coherent energy is transformed progressively into incoherent energy, except for $L/l_s \sim 1$ [Fig. 4(a)], where we may still distinguish some coherent echoes.

In relatively thin samples ($L/l_s = 3$), both coherent and incoherent energies are still present [as illustrated in Figs. 3(b) and 5(b)]. The early energy-density profiles at short times are still controlled by the ballistic (coherent) energy pulse. Because of boundary (internal) reflection, tail evolution of the ballistic δ -like pulse towards longer time (in the region of incoherent scattered coda) is qualitatively different between slab and cylindrical geometries [Fig. 4(b)]. In the cylinder, we still observe a ballistic peak and a diffusivelike peak, as in the infinite medium, which is modulated in between by reverberating coherent pulses from the lateral wall (with an oblique incidence).

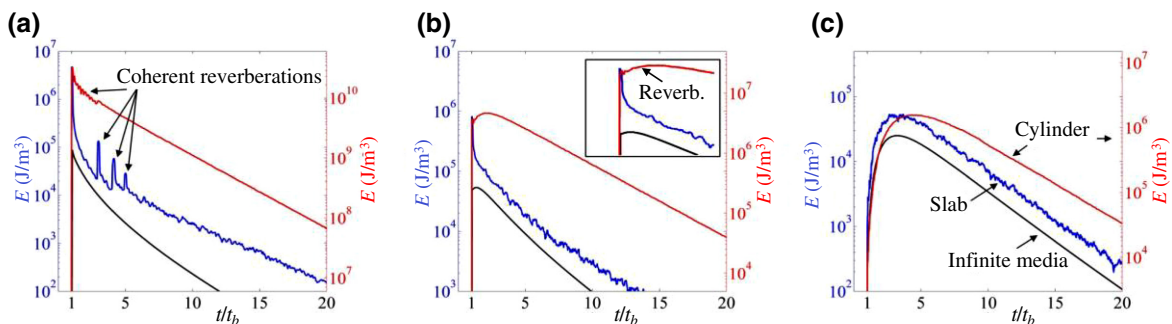


FIG. 4. Comparison of temporal energy-density profiles obtained with simulations in finite-size media (red for cylinder and blue for slab) and with the RTE solution in infinite media (black) for a point source. Three panels correspond to different scattering samples with (a) $L/l_s = 1$, (b) $L/l_s = 3$, and (c) $L/l_s = 10$. Energy densities in cylindrical samples are about 1 order of magnitude higher than those in the slabs due to constrained energy spreading in the lateral direction. Inset (b), reverberations between ballistic and diffusion peaks.

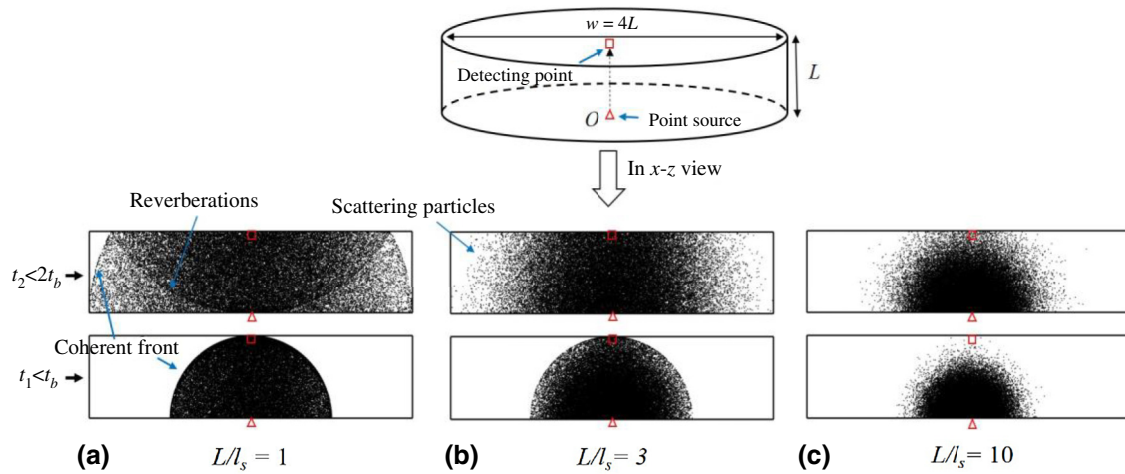


FIG. 5. Similar simulations to those in Fig. 3 but through a slab sample of width (diameter) $w = 4L$ (L being thickness).

On the contrary, for the thin slab, two peaks in the early energy-density profile merge into a single ballisticlike one, suppressing, accordingly, the minimum in the energy density resulting from single forward scattering [17]. Such a modified profile turns out to be very similar to that observed with a sample of $L/l_s = 1$ [Fig. 4(a)], which could lead to an overestimation of l_s by a factor of 3 (error of $\sim 200\%$).

Zhang and Zhang [33] have highlighted the anomalous diffusive behavior in the thin slab geometry ($L/l_s < 3$) with internal reflections. By studying the decay time, τ_D (referred to as the Thouless time), of the transmitted energy-density profile at long times, a diffusion constant, $D_0 (= Vl^*/3)$, can be inferred via the diffusion model [8,23,33]:

$$I(L, t) \sim \exp(-t/\tau_D) = \exp[-\pi^2 D_0 t / (L + 2z_e)^2]. \quad (4)$$

In their study, the intrinsic attenuation (absorption) of about $\exp(-t/\tau_a)$ is neglected, since the absorption time, $\tau_a (= Q_i/\omega)$, is much larger than that of τ_D inferred from Eq. (4). z_e is an extrapolation length deduced from the boundary conditions for the diffusion equation and is related to internal reflection through $z_e = (2/3)l^*(1 + \langle R \rangle)/(1 - \langle R \rangle)$, with $\langle R \rangle$ as the angle-averaged reflection coefficient. However, the diffusion constant, $D_0(L)$, derived from first-principles calculations (Bethe-Salpeter equation) is found to increase with decreasing L , up to 45% at $L \approx 2l_s$. Another observation is the change in scaling between the source-receiver distance, L , and the early arrival time, t_p , of the peak for the thin slab: the transition from $t \sim L$ (ballistic regime) to $t \sim L^2$ (diffusive regime) is no longer well identified at around $L/l_s \sim 3$. Such anomalous transport behavior in thin samples is ascribed to the wave-focusing effect due to boundary (internal) reflections,

which concentrate the wave energy in the forward direction and make the randomization of propagation direction more difficult [33].

For the finite samples considered here (slab and cylinder) with perfect reflection, $\langle R \rangle = 1$ [z_e and $\tau_D \rightarrow \infty$ according to Eq. (4)], the time-dependent energy-density profiles should tend to nonzero asymptotic values at long times due to energy conservation. This is confirmed by Fig. 6(a), in which we plot the results of MC simulations without intrinsic attenuation in a thin slab of $L/l_s = 3$ and a thick slab of $L/l_s = 10$ (diffusive regime). Therefore, the decays of the transmitted coda at long times are mostly governed by the absorption time, τ_a (or quality factor Q_i), in this study.

Nevertheless, for a thin slab, the wave focusing in the forward direction, due to internal reflections (as mentioned above), may lead to cancellation of the minimum in the transmitted profile (for $L/l_s > 2.4$) predicted at short times [17], merging the ballistic peak and the diffusion one into a single ballisticlike peak (the ballistic pulse amplitude is also doubled by the boundary effect, as in Ref. [22]). This can lead to the mistaken inference of l_s with a huge overestimation (mentioned above) and provides a possible explanation for the uncertainty in peak-position determination observed previously [33].

Such a wave-focusing effect should be particularly pronounced at normal incidence, as occurring on the top and bottom surfaces of a slab (for on-axis detection), in comparison with what is happening mostly at oblique incidence from the lateral wall of a cylinder. To confirm this idea, we conduct off-axis detection in the thin slab of $L/l_s = 3$ at a distance of $r_{\text{off}} (= l_s, 2l_s, \text{ and } 3l_s)$ from the epicenter. As shown in Fig. 6(b), the on-axis energy-density profile exhibits a single peak, while the profile for off-axis detection recovers two peaks at short times ($t > t_b$), such as those observed in infinite media for a source-receiver distance of $L > 2.4l_s$ (Fig. 1).

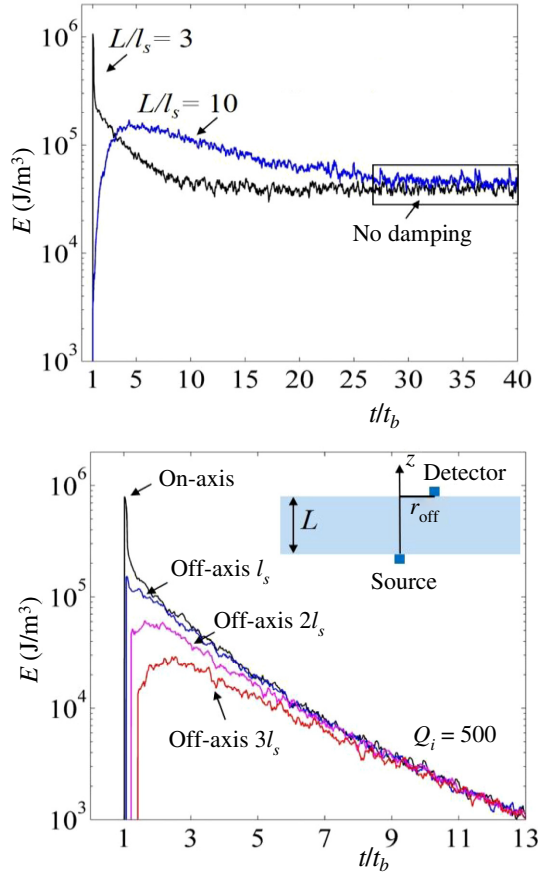


FIG. 6. (a) Time profiles of energy density in optically thin ($L/l_s = 3$) and thick ($L/l_s = 10$) samples without absorption ($Q_i = \infty$). (b) Time profiles in the thin sample in the presence of absorption ($Q_i = 500$) for on-axis and off-axis detections.

D. Inverse problem with a two-parameter RTE

The above investigation of the direct wave-transport problem in finite-size samples (cylinder and slab) in the presence of boundary reflections demonstrates that wave transport in the multiple-scattering regime can be characterized based on the RTE solved by MC simulations with two free parameters (Q_i^{-1} and l_s or Q_s^{-1}). More precisely, we can infer the intrinsic attenuation, Q_i^{-1} , via decay at long times of the coda by a best fit of simulated energy-density profiles to the experimental one (see experiments

in Sect. IV) whereas we can deduce the scattering mean free path, l_s , by the adjustment of profiles at short times. Particular attention must be paid to the presence of ballistic and diffusive peaks for the thin slab, $L/l_s \geq 3$, with complementary off-axis detection, if necessary.

To quantitatively estimate the effect of boundary reflections, we calculate the difference between the exact (simulations in finite samples) and approximate (simulations in infinite media) solutions to infer the intrinsic attenuation, Q_i^{-1} , and the scattering attenuation, Q_s^{-1} (or l_s). To do so, we seek to adjust the energy-density profiles obtained from MC simulations of finite samples (with given Q_i^{-1} and l_s) with the approximate analytical RTE solution [Eq. (3)] by the fitting process described above.

Table I lists these newly derived values of Q_i^{-1} and l_s in cylindrical and slab samples for normalized source-receiver distances of $L/l_s = 3$ and 10 [Figs. 4(b) and 4(c)]. For intrinsic attenuation, the apparent Q_i^{-1} appears to be smaller due to boundary reflections, which prevent the spreading of energy radiation (Figs. 3 and 5). Compared with the reference (given) values, the derived Q_i^{-1} values are consequently underestimated by 25% to 35%, except for the thick slab, $L/l_s = 10$, where the decay rate is almost the same as that in an infinite medium. For the scattering mean path, the derived l_s values are underestimated by 50% and 25% in small ($L/l_s = 3$) and long ($L/l_s = 10$) cylindrical samples, respectively. For slab samples, no significant deviation is observed in the thick-sample case ($L/l_s = 10$), while in the relatively thin slab ($L/l_s = 3$) we need to pay attention to the comparison due to the anomalous behavior observed for on-axis detection. As indicated by Fig. 6(b), this issue may be fixed by using off-axis detection in numerical simulations and experiments for inverse-problem applications (see discussion in Sec. IV B).

III. MC SIMULATIONS OF RADIATION TRANSPORT FROM A FINITE-SIZE SOURCE

A. Finite-size source

For a consistent comparison with experimental observations, we also have to take into account the finite-size character of the source. In the diffusive regime, the energy-density profile resulting from a point source can be compared with that from plane-wave excitation [8], by using

TABLE I. Deviation of inferred values of l_s and Q_i^{-1} when the boundary reflection effect is ignored.

L/l_s	l_s (mm)	Q_i^{-1}	$l_{s\text{inferred}}$ (mm)	$Q_{i\text{inferred}}^{-1}$	$\Delta l_s/l_s$ (%)	$\Delta Q_i^{-1}/Q_i^{-1}$ (%)
Cylinder	3	2×10^{-3}	1.5	1.3×10^{-3}	-55	-35
	10	2×10^{-3}	0.75	1.5×10^{-3}	-25	-25
Slab	3	2×10^{-3}	10	1.3×10^{-3}	200	-35
	10	2×10^{-3}	1.0	2×10^{-3}	0	0

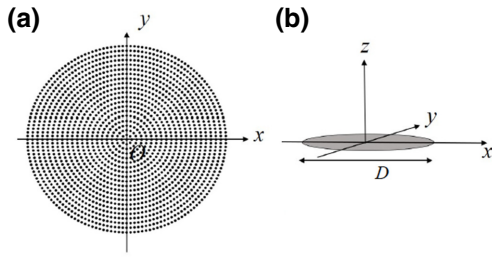


FIG. 7. (a) Finite-size source made of $M = 20$ concentric circles with a radius $r = (D/2) = 12.5$ mm. (b) Side view.

three-dimensional and one-dimensional solutions [similar to Eq. (3)] of the diffusion equation. The shapes of the energy-density profiles are found to differ noticeably: the transmitted profile for a plane-wave source is longer than that obtained with a pointlike source and reaches its peak value at a later time, due to a larger contribution from sound traveling over longer paths from the plane-wave source.

Within the frame of the RTE, we can similarly integrate the solution [Eq. (3)] for a source centered at point $P_0 (x_0, y_0, z_0)$ over its extension in the x - y plane at $z = 0$ [Fig. 2(a)]. Using the MC simulation, we design a finite-size source by regularly placing an

array of incoherent point sources (incoherent radiation) in concentric circles [Fig. 7(a)]. This finite-size source comprises $N_p = 4M^2 + 4M + 1$ point sources placed on $M = 20$ concentric circles centered at O . The m th concentric circle radius is mr_Δ ($1 \leq m \leq M$), such that the source radius is $r = D/2 = Mr_\Delta$. The coordinates of the point sources are given by $[x_0 + mr_\Delta \cos(\pi n/4m), y_0 + mr_\Delta \sin(\pi n/4m), z_0]$ ($0 \leq m \leq M, 0 \leq n \leq 8m - 1$ for $m > 0$). If each point source emits N particles, the whole source shoots $N_{\text{tot}} = N_p N$ particles. By setting the source size equal to the sample diameter ($D = w$), we can recover a quasi-one-dimensional geometry, i.e., a plane-wave source-radiation problem.

B. Three-dimensional infinite media

Figure 8 compares the simulated energy-density profiles in three infinite media (with different l_s) from a point source, a small source $D = L/4$ ($= 2.5$ mm), and a large radiation source $D = 4L$ ($= 40$ mm), which are detected at a fixed source-receiver distance of $L = 10$ mm on the z axis [Fig. 7(b)]. The profiles obtained with a small radiation source coincide with those from a point source, suggesting the validity of a pointlike source model when the source size is much smaller than source-receiver distance L .

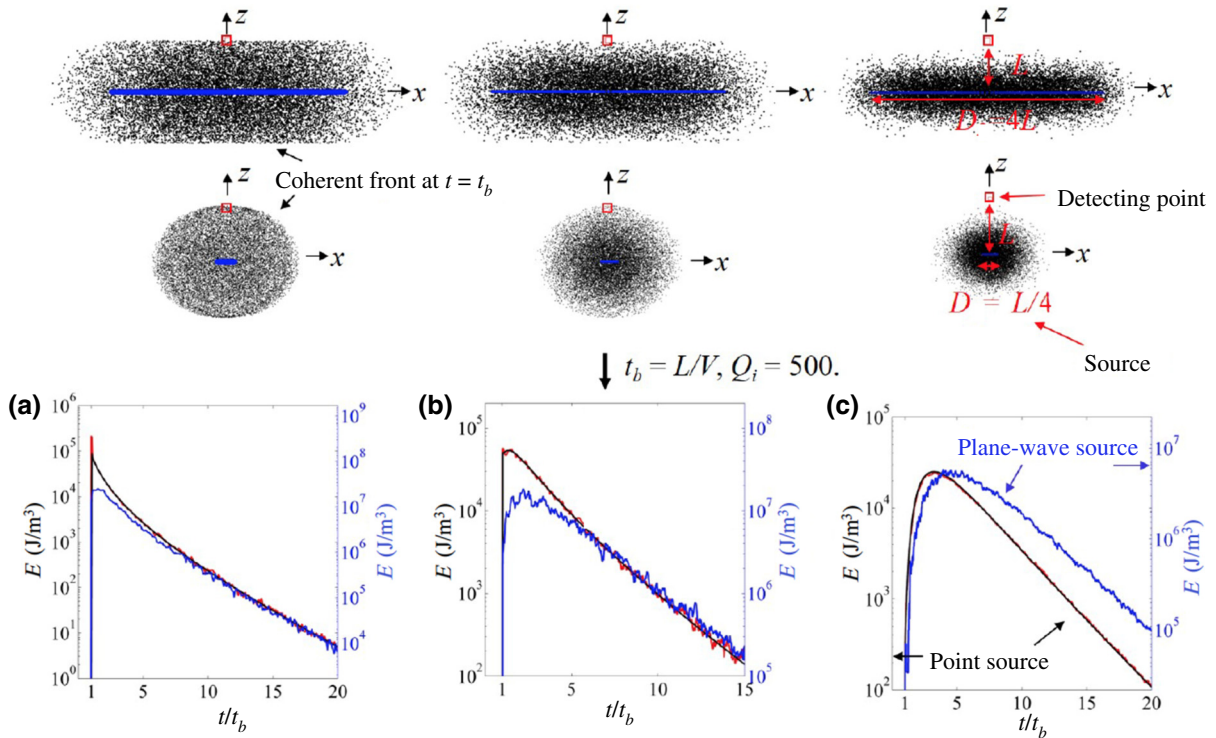


FIG. 8. Simulations in infinite media for different source sizes at a fixed distance. Energy-density profiles for the point source (black) coinciding with those for a small source of $D = L/4$ (red) but are about 1 order of magnitude larger than those for a large source of $D = 4L$ (blue). Three panels (a), (b) and (c) correspond to different scattering samples with $L/l_s = 1, 3$ and 10 , respectively (similar to Figs. 3 and 5).

TABLE II. Deviation of inferred values of l_s and Q_i^{-1} due to the large source size.

L/l_s	l_s (mm)	Q_i^{-1}	$l_{s\text{inferred}}$ (mm)	$Q_{i\text{inferred}}^{-1}$	$\Delta l_s/l_s$ (%)	$\Delta Q_i^{-1}/Q_i^{-1}$ (%)
3	3.3	2×10^{-3}	1.6	1.9×10^{-3}	-52	-5
10	1.0	2×10^{-3}	0.7	1.7×10^{-3}	-30	-15

For the large radiation source, the obtained energy-density profile in the diffusive regime ($L/l_s = 10$) is very close to that for a plane-wave source with the peak shifting at a late time due to a larger contribution from acoustic waves traveling over longer paths compared with those from a point source [8]. Moreover, the appearance of a diffusionlike peak at a short distance, $L/l_s = 1$, is likely to be due to the edge- (point-) source radiation, the distance of which to the receiver is larger than $3l_s$. If one ignores the effect of source size, particularly in the plane-source geometry ($L \leq D_2/4$), and seeks to fit the corresponding energy-density profiles (numerical or experimental) with the RTE solution for a point source, then the deduced scattering mean free path, l_s , and the intrinsic attenuation, Q_i^{-1} , can be significantly underestimated due to the longer coda signals (Table II).

C. Three-dimensional finite media

Figure 9 displays the simulated energy-density profiles for the planar radiation source, $D = w$, in both the cylindrical ($L > w$) and slab samples ($L < w$). These profiles look the same shape but with different magnitudes due to the respective input energy. Indeed, under the planar-radiation-source geometry, one recovers

a quasi-one-dimensional energy-transport problem. Most interestingly, we observe the reappearance of the diffusion peak in thin samples with $L/l_s = 3$ [Fig. 9(b)]. Similar to off-axis detection [Fig. 8(b)], the dominant oblique incidence at the on-axis detector (plane) for a large or plane-wave source reduces significantly the wave-focusing effect by boundary reflection in the forward direction [33].

Table III illustrates again the possible deviation of l_s and Q_i^{-1} inferred from the approximate analytical RTE solution in an infinite medium for point-source radiation. Combined effects of the boundary reflection and the source size may lead to underestimated values of both l_s and Q_i^{-1} from their real values, which is even more pronounced in thin samples (up to 40%) than in thick samples (in the diffusive regime). Clearly, the exact solution of the RTE through MC simulations in the presence of boundaries is of primordial importance to infer quantitatively l_s and Q_i^{-1} from experimental data obtained for finite-size samples, as we show in the following section.

IV. EXPERIMENTS

A. Dry granular materials

We compare simulated energy profiles and experimental ones in dry glass-bead packing materials, where elastic

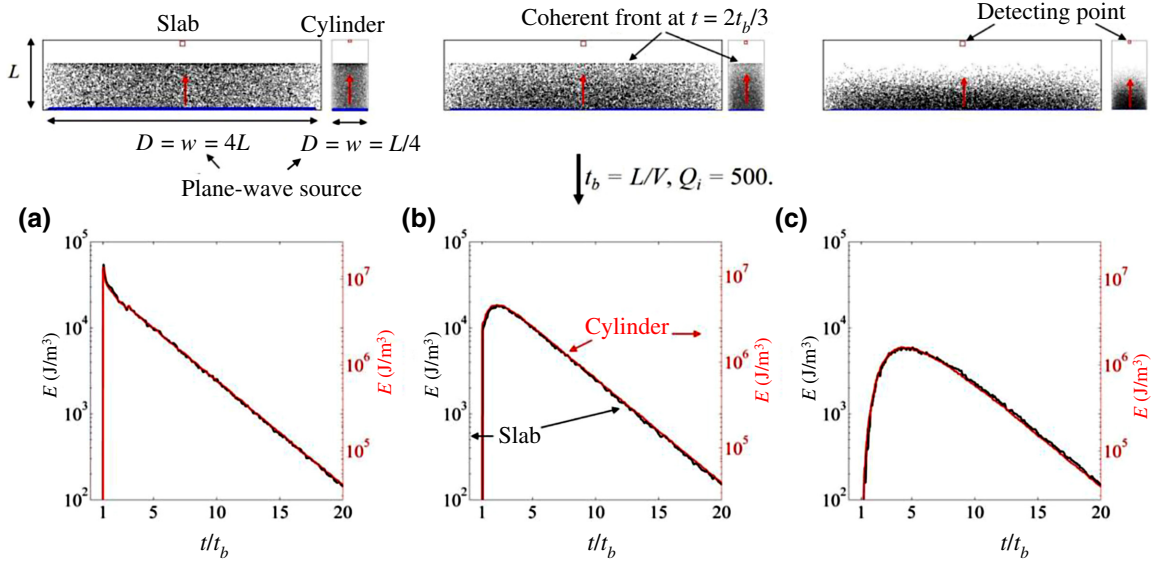


FIG. 9. Simulations of the energy-density profile in finite-size media for a plane-wave source. (a)–(c) Different scattering samples (similar to Figs. 3, 5, and 8) with $L/l_s = 1, 3$ and 10 , respectively, in which red curves refer to cylinders and black ones to slabs. Snapshots are recorded at instant $t = 2t_b/3$. Profiles are the same shape but of different magnitude due to radiation intensity.

TABLE III. Deviation of inferred values of l_s and Q_i^{-1} due to the boundary reflection and source size.

L/l_s	l_s (mm)	Q_i^{-1}	$l_{s\text{inferred}}$ (mm)	$Q_i^{-1\text{inferred}}$	$\Delta l_s/l_s$ (%)	$\Delta Q_i^{-1}/Q_i^{-1}$ (%)
3	3.3	2×10^{-3}	1.8	1.25×10^{-3}	-45	-37.5
10	1.0	2×10^{-3}	0.7	1.5×10^{-3}	-30	-25

waves propagate through a very heterogeneous contact network. In such strong-scattering media, analytical solutions of the diffusion equation fit well with experimental data with appropriate boundary conditions under the assumption of a plane-wave source excitation [36]. Hence, a comparison of experimental data to numerical RTE solutions by the MC method provides a benchmark to ensure the validity of our simulations.

Our ultrasound scattering experiments are conducted on packed dry glass beads with diameter $d \sim 0.7$ mm. They are confined in two duralumin cells with respective diameters of $w = 30$ and 60 mm and filled to a height of $L = 7.4$ or 11.4 mm, with a solid volume fraction of about 0.63. A large longitudinal piezoelectric transducer of diameter $D = 30$ mm (plane-wave source) is placed on the bottom, and a small detector of diameter in 2 mm is placed on top of the granular sample [Fig. 10(a)]. A five-cycle tone burst centered at 500 kHz is applied to the source transducer. Statistically independent packing configurations are realized by stirring glass beads vigorously after each ultrasonic measurement and

compressing the sample again by an axial pressure of $P = 650$ kPa.

Figure 10(b) depicts typical ultrasound signals transmitted in a granular sample of diameter $w = 60$ mm and thickness $L = 7.4$ mm. They are composed of low-frequency (approximately 70 kHz) compressional- (P) and shear- (S) wave pulses propagating ballistically at a velocity of $V_p \approx 1000$ m/s and $V_s \approx 450$ m/s and of high-frequency (approximately 500 kHz) incoherent signals resulting from multiple scattering by the contact-force chains [9]. In the diffusive regime, the ratio, K , of the energy densities contained in the shear (E_S) and compressional (E_P) waves is governed by an equipartition relation, $K = E_S/E_P = 2(V_P/V_S)^3$ [15], thus indicating the dominance of the S wave in incoherent coda signals. Additionally, there is a large impedance mismatch between the granular sample and the duralumin cell (by a factor of more than 10), giving rise to an angle-averaged reflection coefficient, $\langle R \rangle \approx 0.95$, at the cell boundary [36] very close to the total-reflection assumption used in our simulations.

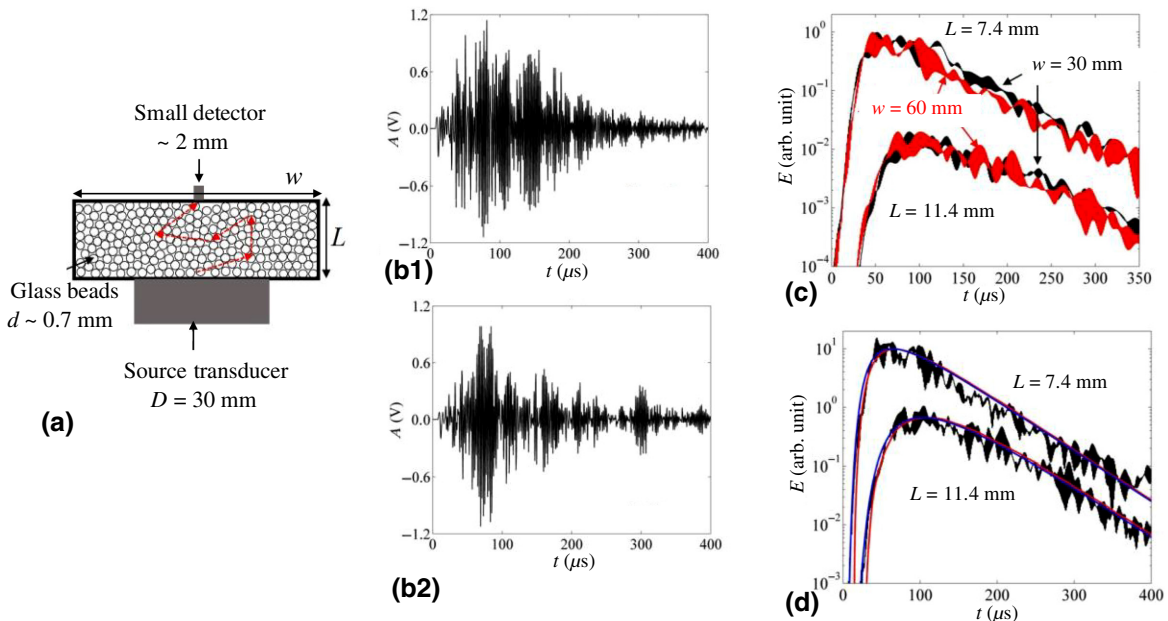


FIG. 10. (a) Schematic illustration of ultrasonic experiments in confined granular materials. (b) Ultrasonic signals transmitted through two different packing configurations. (c) Ensemble-averaged energy profiles measured in a large and a small cell (granular sample), with $w = 60$ (red curves) and 30 mm (black curves) and two different thicknesses L . (d) Comparison between experimental data obtained in the small cell ($w = 30$ mm) and the simulated energy-density profiles (red curves), as well as solutions of the diffusion solution with a plane-wave source (blue curves).

Figure 10(c) shows the ensemble-averaged energy profiles obtained from the square of incoherent signals after high-pass filtering ($f \geq 300$ kHz) obtained for the large ($w = 60$ mm) and small ($w = 30$ mm) granular samples and two different source-receiver distances, $L = 7.4$ and 11.4 mm. From the same finite-size source excitation, no significant difference is observed between the large and small granular packings in this diffusive regime. Indeed, both solutions of the diffusion equation (blue curves) [36] and the MC simulations (red curves) for a plane-wave radiation source provide very satisfactory fits to experimental data (for $D = 30$ mm) with a single set of fit parameters, $l_s = 0.87$ mm and $Q_i^{-1} = 5.9 \times 10^{-3}$ [Fig. 10(d)]. The resulting ratios of $L/l_s \approx 8.5$ and 13 for the two investigated sample thicknesses confirm the validity of the diffusion approximation. Note, however, that the fit with the RTE solution in infinite media from a point source would give $l_s = 0.79$ mm and $Q_i^{-1} = 4.3 \times 10^{-3}$, which are underestimated by 10% and 30%, respectively, compared

with the parameters inferred from our simulations. Since $L < w$ in these samples, the deviations in l_s and Q_i can be mainly ascribed to the effect of the finite-size source (large transducer).

B. Heterogeneous rocks

Our ultimate goal is to apply our inverse method to characterize ultrasound scattering and absorption (intrinsic attenuation) in heterogeneous materials, such as polycrystals [7,28,34]. Here, we pay particular attention to the transition from the ballistic to the diffusive regime. Granite is a typical polycrystal in natural rocks. Figure 11(a) shows a granite slab with dimensions $1 \times 1 \times 0.07$ m³ ($h \approx 7.1$ cm), which is essentially composed of quartz, biotite, and feldspar [Figs. 11(b) and 12(a)]. These crystallites or clusters are on a millimeter scale without specific orientation. For the sake of simplicity, we consider this granite sample to be an isotropic random medium.

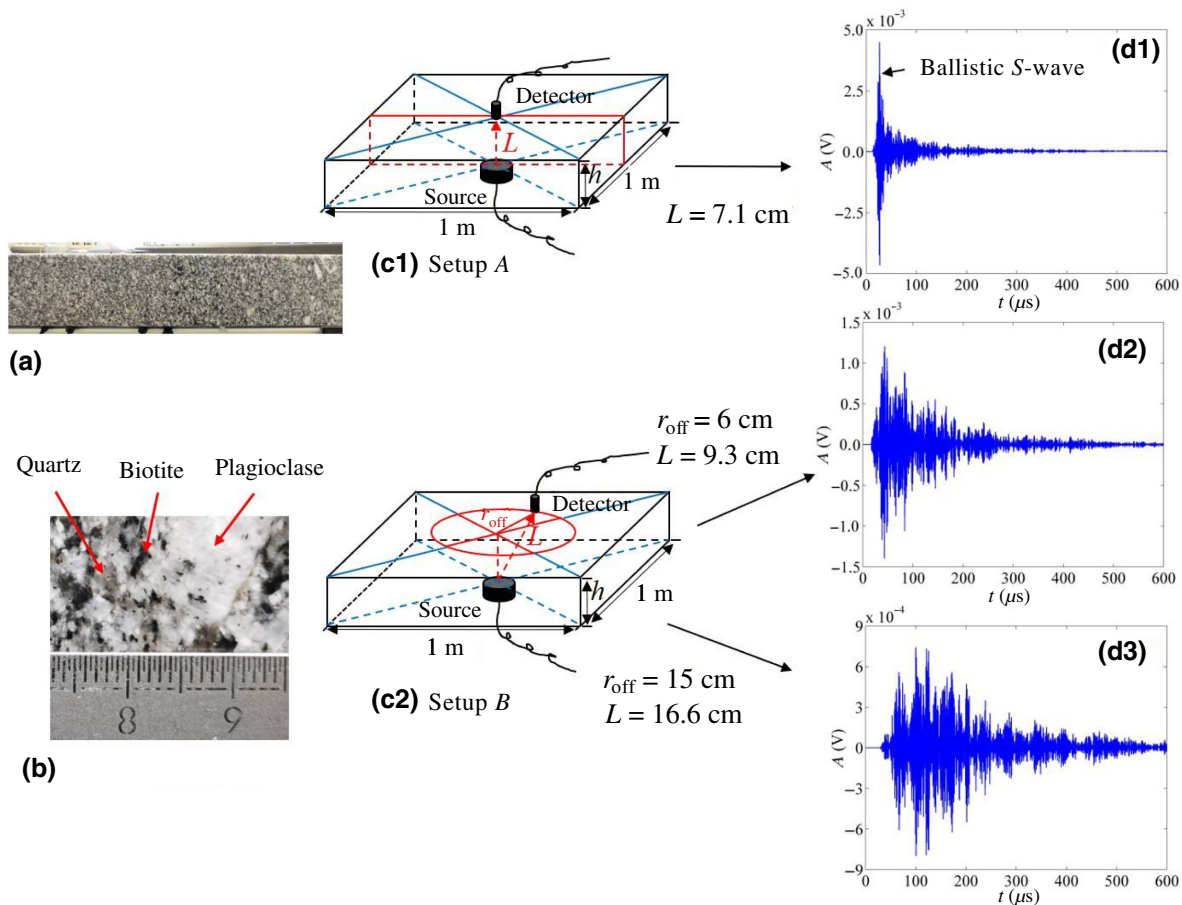


FIG. 11. Ultrasonic experiment on a granite slab. (a) Photograph of the granite slab. (b) Mineral constituents of granite. (c1) Setup A, in which a detector is placed at the opposite end to the source axis. (c2) Setup B, in which a detector is placed on a concentric circle at the opposite end. (d1) Typical transmitted signal recorded with setup A. (d2) Typical transmitted signal recorded with setup B and $r_{\text{off}} = 6$ cm. (d3) Typical transmitted signal recorded with setup B and $r_{\text{off}} = 15$ cm.

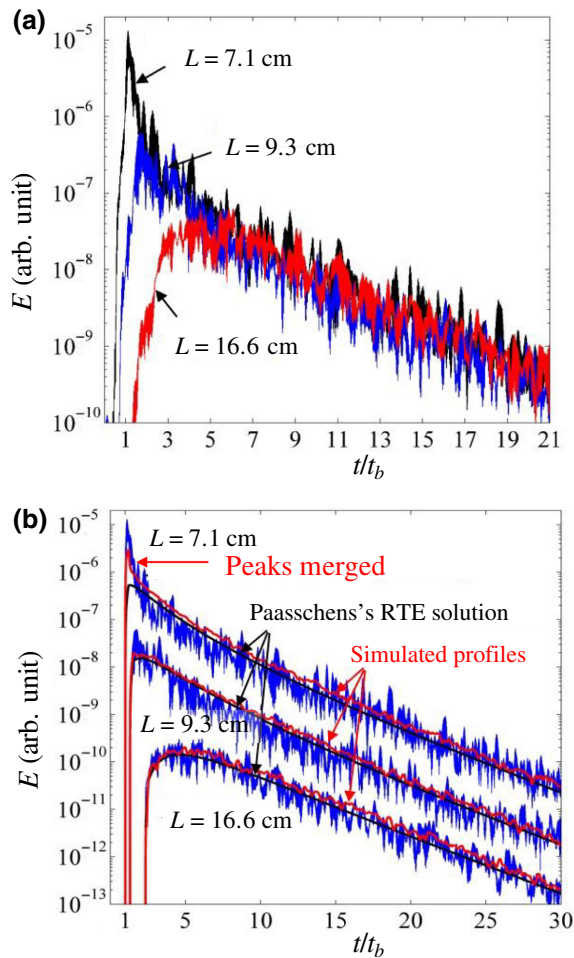


FIG. 12. (a) Ensemble-averaged energy profiles (black, blue, and red) obtained for geometries depicted in Fig. 11(d1)–(d3), respectively. (b) Normalized ensemble-averaged energy profiles (blue) truncated before $t = L/V_s$, fitted by the simulated profiles (red), and the RTE solution in an infinite medium (black).

1. Ultrasonic measurements

Figure 11(c) shows the two setups (*A* and *B*) for the scattering experiment in this granite sample. A large shear-wave transducer of diameter $D = 15$ mm and a small detector of diameter 2 mm are coupled to the bottom and top surfaces, respectively, of the granite slab. The transducer source is excited by a five-cycle tone burst centered at 1 MHz.

In setup *A*, the source and the detector are on the same (*z*) axis perpendicular to the granite surface. To obtain an ensemble of independent configurations for this on-axis measurement, we move both the source and the detector in the plane parallel to the granite slab by steps of 1 cm, i.e., larger than the shear wavelength, $\lambda_s \approx 3.2$ mm ($= V_s/f$, where V_s is the shear-wave velocity, see below). In setup *B*, the off-axis measurements [cf. Fig. 6(b)] are conducted by moving the detector along two circles centered on the *z* axis with radius $r_{\text{off}} = 6$ and 15 cm, respectively. With an

angular step of 22.5° , measurements with 16 independent configurations are conducted.

Figure 11(d1) shows a typical on-axis ultrasonic signal (setup *A*), whereas Figs. 11(d2) and (d3) depict measured off-axis signals (setup *B*). Through an ensemble average of temporal (field) signals over 16 independent configurations, we can cancel out incoherent coda signals and enhance coherent ballistic waves (not shown), which allows *P*- and *S*-wave velocities to be adequately measured. We find, respectively, $V_p \approx 5600$ m/s and $V_s \approx 3200$ m/s. To obtain the energy-density profiles shown in Fig. 12(a), we square the ultrasonic field signals before the ensemble average.

Figure 12(b) illustrates the energy profiles truncated by removing the signal before the arrival of the shear ballistic wave and deconvoluted with the envelop of the input-source energy. As discussed above for the early part of the simulated profiles [Fig. 4(b)], the absence of the diffusion peak in the energy-density profile is experimentally observed again for on-axis detection at $L/l_s \approx 2.5$, which confirms the crucial role of the wave-focusing effect on a thin slab with multiple scattering. As mentioned above, without additional off-axis detection, a highly underestimated value of l_s (200%) would be inferred from the fit of the on-axis-detected profile (setup *A*). For comparison, we also plot the three profiles with analytical RTE solutions in infinite media with $L = (h^2 + r_{\text{off}}^2)^{1/2}$ from a point-radiation source. As expected, they do not reveal any anomalous behavior for on-axis detection at $L/l_s \approx 2.5$ within the multiple-scattering regime [17]. Their best fit to the two profiles measured at $L/l_s \approx 9.2$ and 16.6 in the diffusive regime allows a very similar $l_s \approx 2.8$ cm but slightly higher $Q_i \approx 550$ (about 10%) values to be inferred, due to neglecting reflection effects.

2. Image analysis

To further confirm the consistency of our inverse method, we compare the results of the wave-transport investigation to those of the image analysis of material heterogeneities. More specifically, the correlation length of elastic heterogeneity (or wave velocity) in space can be deduced from a grayscale image of granite [Fig. 13(a)], via an autocorrelation function (ACF) of exponential-type, $R(\mathbf{r}) = \varepsilon^2 \exp(-|\mathbf{r}|/a)$, where a is the correlation length and ε is the standard deviation of shear-wave velocity V_s [6,47].

To this end, a segmented image based on the mineral composition is first derived, as in Fig. 13(b), according to the grayscale value of minerals [48]. We may then assign a velocity value to a pixel, according to known mineral velocities [6], and obtain consequently a spatial distribution of the shear-velocity fluctuation, $\zeta(\mathbf{r})$ [Fig. 13(c)], defined by $V_s(\mathbf{r}) = V_0[1 + \zeta(\mathbf{r})]$ (with V_0 as the mean shear-wave velocity). From $\zeta(\mathbf{r})$, we may derive the above

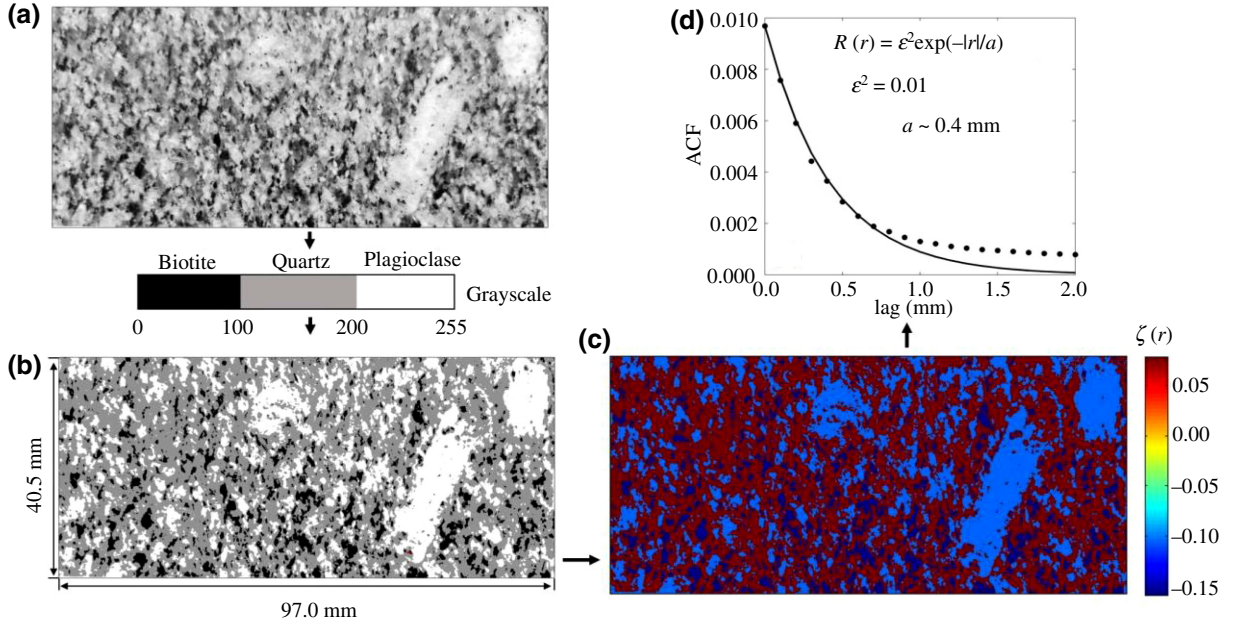


FIG. 13. Evaluation of correlation length from a photographic image of granite. (a) Grayscale image. (b) Segmented image with biotite (black), quartz (gray), and plagioclase (white). (c) Picture of the spatial distribution of shear-wave velocity fluctuations, $\zeta(\mathbf{r})$, around mean velocity $V_0 \approx 3800$ m/s with standard deviation $\varepsilon \approx 0.1$. (d) Estimated autocorrelation function (dots) from the map of shear-velocity fluctuations in (c) and best-fitted exponential-type ACF (solid line).

autocorrelation function, $R(\mathbf{r})$, of velocity fluctuation, $\zeta(\mathbf{r})$, as shown in Fig. 13(d), from which we deduce the parameters $\varepsilon \approx 0.1$ and $a \approx 0.4$ mm for our granite sample. Moreover, we may also infer a mean shear-wave velocity, $V_0 \approx 3800$ m/s, from the spatial distribution of $V_s(\mathbf{r})$, which is 19% higher than the measured S -wave velocity, V_s . Such a discrepancy may be ascribed to the presence of microcracks at the grain boundary, which cannot be accounted for in this image analysis.

Starting from the ACF $R(\mathbf{x})$ discussed above, Sato *et al.* [18] (Chap. 4) have derived an analytical expression for the scattering mean free path based on the Born approximation to study wave scattering (field) by random-velocity fluctuations:

$$l_s = \frac{(1 + 4a^2k^2)}{8\varepsilon^2a^3k^4}, \quad (5)$$

as a function of a , ε , and $k = 2\pi f/V_0$ (the shear-wave number for the scalar case considered here for $f = 1$ MHz). Using the fit parameters of a and ε and the measured V_0 (≈ 3200 m/s), we may obtain from Eq. (5) an estimated value of $l_s \approx 4.6$ cm, which is fairly consistent with the value of $l_s \approx 2.8$ cm inferred by our MC method. We believe that the larger value (about 60%) derived from Eq. (5) is mainly due to the single-scattering approximation, as well as possible scattering by some microcracks not considered here.

V. CONCLUSION

We develop an efficient inverse method to deduce the intrinsic attenuation, Q_i^{-1} , and the scattering mean free path, l_s , of ultrasound in finite heterogeneous materials with boundary reflections. To fit the experimental shear-coda-wave profiles, we solve the acoustic radiative-transfer equation by Monte Carlo simulations with various sample geometries and radiation sources. Particular attention is paid to the transition from the ballistic to the diffusive regime as a function of normalized source-receiver distance, L/l_s . Boundary reflection induces a larger contribution of acoustic waves traveling over longer paths compared with the case of an infinite medium. Accordingly, the transmitted profile is noticeably longer than that obtained in an infinite medium and reaches its diffusionlike peak value at a later time, together with a smaller decay rate in the late coda. As a consequence, the values of Q_i^{-1} and l_s deduced from fitting with the RTE in an infinite medium are underestimated by up to 40%. A similar situation occurs when the finite-size character of the source is not taken into account in the fitting procedure.

Most importantly, we find, based on both MC simulations and experiments on thin (granite) samples with $L/l_s \sim 3$, that internal reflections may cause anomalous behavior in the case of on-axis detection. Indeed, a wave-focusing effect can occur in the forward direction at nearly normal incidence, which makes the randomization of wave propagation more difficult during the scattering process. This affects fundamentally the time profile of energy

density at an early time, with the ballistic and diffusion peaks being merged, which can lead to an overestimation of I_s by more than 200%. We show that such a mistaken inference can nevertheless be avoided by off-axis detection.

Further investigation would be needed to include anisotropic scattering, wave-mode conversion, and variable reflection coefficients in the MC simulation to compare more quantitatively results from MC simulations with ultrasound spectroscopic measurements in granular porous rocks and polycrystals. We will also extend our investigation to other scattering media dominated by microcracks.

ACKNOWLEDGMENTS

This work is supported by the National Natural Science Foundation of China (Grant No. 41821002), the 111 projects “Deep-Superdeep Oil & Gas Geophysical Exploration” (Grant No. B18055), the French LABEX WIFI under Grants No. ANR-10-LABX-24 and No. ANR-10-IDEX-0001-02 PSL, and the Public Applied Technology Research Programs of Zhejiang Province of China (Grant No. LGF20F020008).

-
- [1] K. W. Winkler and A. Nur, Seismic attenuation: Effects of pore fluids and frictional-sliding, *Geophysics* **47**, 1 (1982).
- [2] R. E. Sheriff, Factors affecting seismic amplitudes, *Geophysical Prospecting* **23**, 125 (1975).
- [3] M. N. Toksöz, D. H. Johnston, and A. Timur, Attenuation of seismic waves in dry and saturated rocks; I, laboratory measurements, *Geophysics* **44**, 4 (1979).
- [4] K. W. Winkler and T. J. Plona, Technique for measuring ultrasonic velocity and attenuation spectra in rocks under pressure, *J. Geophys. Res.* **87**, B13 (1982).
- [5] N. Lucet and B. E. Zinszner, Effects of heterogeneities and anisotropy on sonic and ultrasonic attenuation in rocks, *Geophysics* **57**, 8 (1992).
- [6] Y. Fukushima, O. Nishizawa, H. Sato, and M. Ohtake, Laboratory study on scattering characteristics of shear waves in rock samples, *Bull. Seismol. Soc. Am.* **93**, 1 (2003).
- [7] R. L. Weaver, Diffusivity of ultrasound in polycrystals, *J. Mech. & Phys. Solids* **38**, 1 (1990).
- [8] J. H. Page, H. P. Schriemer, A. E. Bailey, and D. A. Weitz, Experimental test of the diffusion approximation for multiply scattered sound, *Phys. Rev. E* **52**, 3 (1995).
- [9] X. Jia, C. Caroli, and B. Velicky, Ultrasound Propagation in Externally Stressed Granular Media, *Phys. Rev. Lett.* **82**, 9 (1999).
- [10] A. Tourin, M. Fink, and A. Derode, Multiple scattering of sound, *Waves in Random Media* **10**, 345 (2000).
- [11] T. Brunet, X. Jia, and P. Mills, Mechanisms for Acoustic Absorption in Dry and Weakly Wet Granular Media, *Phys. Rev. Lett.* **101**, 138001 (2008).
- [12] P. Anugonda, J. S. Wiehn, and J. A. Turner, Diffusion of ultrasound in concrete, *Ultrasonics* **39**, 6 (2001).
- [13] R. Thery, A. Guillemot, O. Abraham, and E. Larose, Tracking fluids in multiple scattering and highly porous materials: Toward applications in non-destructive testing and seismic monitoring, *Ultrasonics* **102**, 106019 (2019).
- [14] R. Snieder and J. Page, Multiple scattering in evolving media, *Phys. Today* **60**, 49 (2007).
- [15] L. Ryzhik, G. Papanicolaou, and J. B. Keller, Transport equations for elastic and other waves in random media, *Wave Motion* **24**, 4 (1996).
- [16] J. A. Turner and R. L. Weaver, Radiative transfer of ultrasound, *J. Acoust. Soc. Am.* **96**, 6 (1993).
- [17] J. Paasschens, Solution of the time-dependent Boltzmann equation. *Phys. Rev. E* **56**, 1 (1997).
- [18] H. Sato, M. C. Fehler, and T. Maeda, *Seismic Wave Propagation and Scattering in the Heterogeneous Earth* (Springer, Berlin, 2012).
- [19] L. Margerin, Introduction to radiative transfer of seismic waves, *Geophys. Monogr. Am. Geophys. Union* **157**, 229 (2005).
- [20] A. A. Gusev and I. R. Abubakirov, Monte-Carlo simulation of record envelope of a near earthquake, *Phys. Earth Planet. Inter.* **49**, 30 (1987).
- [21] M. Hoshiya, Simulation of multiple-scattered coda wave excitation based on the energy conservation law, *Phys. Earth Planet. Inter.* **67**, 1 (1991).
- [22] M. Hoshiya, Simulation of coda wave envelope in depth-dependent scattering and absorption structure, *Geophys. Res. Lett.* **21**, 25 (1994).
- [23] L. Margerin, M. Campillo, and B. Tiggelen, Radiative transfer and diffusion of waves in a layered medium: New insight into coda Q, *Geophys. J. Int.* **134**, 2 (1998).
- [24] K. Aki and B. Chouet, Origin of coda waves: Source, attenuation, and scattering effects, *J. Geophys. Res.* **80**, 23 (1975).
- [25] H. Sato, Energy propagation including scattering effects: Single isotropic scattering approximation, *J. Phys. Earth.* **25**, 27 (1977).
- [26] J. P. Wesley, Diffusion of seismic energy in the near range, *J. Geophys. Res.* **70**, 20 (1965).
- [27] U. Wegler and B. G. Lühr, Scattering behavior at Merapi volcano (Java) revealed from an active seismic experiment, *Geophys. J. Int.* **145**, 3 (2001).
- [28] J. A. Turner and R. L. Weaver, Radiative-transfer and multiple-scattering of diffuse ultrasound in polycrystalline media, *J. Acoust. Soc. Am.* **96**, 6 (1994).
- [29] T. Bourbie, O. Coussy, and B. Zinszner, *Acoustics of Porous Media* (Edition Technip, Paris, 1987).
- [30] Y. Gueguen and V. Palciauskas, *Introduction to the Physics of Rocks* (Princeton Univ. Press, Princeton, 1994).
- [31] A. Lagendijk, R. Vreeker, and P. D. Vries, Influence of internal reflection on diffusive transport in strongly scattering media, *Phys. Lett. A* **136**, 1 (1989).
- [32] J. Zhu, D. Pine, and D. Weitz, Internal reflection of diffusive light in random media, *Phys. Lett. A* **44**, 6 (1991); R. Elaloufi, R. Carminati, and J.-J. Greffet, Diffusive-to-ballistic transition in dynamic light transmission through thin scattering slabs: a radiative transfer approach, *J. Opt. Soc. Am.* **A21**, 1430 (2004).
- [33] X. Zhang and Z. Q. Zhang, Wave transport through thin slabs of random media with internal reflection: Ballistic to diffusive transition, *Phys. Rev. E* **66**, 016612 (2002).

- [34] J. A. Turner and R. L. Weaver, Time dependence of multiply scattered diffuse ultrasound in polycrystalline media, *J. Acoust. Soc. Am.* **97**, 5 (1995).
- [35] O. Nishizawa and Y. Fukushima, Laboratory experiments of seismic wave propagation in random heterogeneous media, *Adv. Geophys.* **50**, 8 (2008).
- [36] X. Jia, Codalike Multiple Scattering of Elastic Waves in Dense Granular Media, *Phys. Rev. Lett.* **93**, 15 (2004).
- [37] O. Nishizawa, T. Satoh, X. Lei, and Y. Kuwahara, Laboratory studies of seismic wave propagation in inhomogeneous media using a laser Doppler vibrometer, *Bull. Seimol. Soc. Am.* **87**, 809 (1997).
- [38] A. Ishimaru, *Wave Propagation and Scattering in Random Media* (Academic Press, New York, 1978), Vols. 1 and 2.
- [39] P. Sheng, *Introduction to Wave Scattering, Localization and Mesoscopic Phenomena* (Springer, Berlin, 2006).
- [40] S. Torquato, *Random Heterogeneous Materials: Microscopic and Macroscopic Properties* (Springer, New York, 2002).
- [41] R. S. Wu, Multiple scattering and energy transfer of seismic waves—separation of scattering effect from intrinsic attenuation—I. theoretical modeling, *Geophys. J. Int.* **82**, 1 (1985).
- [42] Y. Zeng, F. Su, and K. Aki, Scattering wave energy propagation in a random isotropic scattering medium 1. theory, *J. Geophys. Res.* **96**, B1 (1991).
- [43] S. A. Dupree and S. K. Fraley, *A Monte Carlo Primer, A Practical Approach to Radiation Transport* (Kluwer Academic/Plenum, New York, 2002).
- [44] I. Lux and L. Koblinger, *Monte Carlo Particle Transport Methods: Neutron and Photon Calculations* (CRC Press, Boca Raton, Fla, 1991).
- [45] K. Yoshimoto, Monte-Carlo simulation of seismogram envelope in scattering media, *J. Geophys. Res.* **105**, B3 (2000).
- [46] C. Lacombe, M. Campillo, A. Paul, and L. Margerin, Separation of intrinsic absorption and scattering attenuation from Lg coda decay in central France using acoustic radiative transfer theory, *Geophys. J. Int.* **154**, 2 (2003).
- [47] C. Sivaji, O. Nishizawa, G. Kitagawa, and Y. Fukushima, A physical model study of the statistics of seismic waveform fluctuations in random heterogeneous media, *Geophys. J. Int.* **148**, 3 (2002).
- [48] H. Andrä, N. Combaret, J. Dvorkin, E. Glatt, J. Han, M. Kabel, and M. Marsh, Digital rock physics benchmarks—Part I: Imaging and segmentation, *Comput. Geosci.* **50**, 25 (2013).